



Journal of Applied Sciences

ISSN 1812-5654

science
alert

ANSI*net*
an open access publisher
<http://ansinet.com>

Elastic Analysis of Discontinues Medium using Mesh-Free Method

S.M. Binesh, N. Hataf and A. Ghahramani

Geotechnical Engineering Division, Department of Civil Engineering, School of Engineering,
Shiraz University, Shiraz, 7134851156, Iran

Abstract: In this study, a truly mesh-free method is implemented for the elastic analysis of discontinues media. The media is divided into separate parts which are connected to each other by the interface layers. The displacement field in each part is constructed by the radial basis point interpolation method, enriched by the polynomial terms. The final system of equations is derived by the substitution of the displacement field into the weak form of the governing equation. The dependency of the method on the background mesh has been taken care of by stabilized nodal integration. Based on derived equations a computer code is developed and some cases are investigated. The results of analyses show that the nodal integration improves the accuracy of results in comparison with the Gauss method. The stability of proposed method is also guaranteed by the suitable choice for shape parameters and the radius of supports.

Key words: Discontinues medium, elastic analysis, mesh-free method, nodal integration

INTRODUCTION

Contact problems are very common and hence important in mechanical and civil engineering. Anytime there is an interface between two materials, there is a discontinuity and the usual analytical methods used in continues solid mediums fail. Strong discontinuities can be solved easier by numerical methods than analytical ones. Conventional engineering numerical methods such as Finite Element (FEM) and Finite Difference (FDM) are based on element or mesh and hence may give rise to problems related to mesh distortion. To address these issues many mesh-free methods or element-free methods have been developed in the past few years. To name a few: the Smoothed Particle Hydrodynamics (SPH) method (Lidersky and Petschek, 1991), Element Free Galerkin (EFG) method (Belytschko *et al.*, 1994), Reproducing Kernel Particle Method (RKPM) (Liu *et al.*, 1995), Local Petrov-Galerkin Method (LPGM) (Atluri and Zhu, 1998) and Point Interpolation Method (PIM) (Liu and Gu, 2001). Detailed descriptions and discussions on these mesh-free methods can be found in, for example (Liu, 2003).

There has been a great deal of research into the implementation of the Radial Basis Point Interpolation Method (RBPIM) in many engineering problem solutions. The RBPIM has the following advantages:

- The shape function has the Kronecker delta property

- The moment matrix used in constructing shape functions is always invertible
- The linear consistency is guaranteed by using the RBPIM basis functions enriched with the linear polynomials

The generation of discrete system of equations in the RBPIM, like the majority of mesh-free methods, is based on Galerkin procedure. Gaussian integration is commonly used in Galerkin mesh-free methods for the integration of weak forms and thus a background mesh is needed to perform integration. However the misalignment of the local supports and the integration cells may deteriorate the accuracy of results. Dolbow and Belytschko (1999) investigated this problem and suggested the bounding box technique for the construction of the integration cells which match the shape functions supports. Due to the complexity involved in Gaussian integration, attempts have been devoted to explore stabilized nodal integration methods for Galerkin-based mesh-free methods.

The source of instability in nodal integration is the vanishing of the first derivatives of the shape functions at the nodes. Since the strain energy term in the weak form consists only the first derivatives of shape functions, nodal sampling does not adequately reflect the energy of the short-wavelength mode and its contribution to the stiffness matrix is severely underestimated. This instability is manifested by spurious short wavelength

modes. Randles *et al.* (1999) used the idea of computing derivative away from the centroid of the support domain and proposed a stress point method to improve accuracy and to reduce spurious oscillations in SPH. Bonet and Kulasegaram (1999) introduced an integration correction to stabilize the nodal integration method and to eliminate the spurious modes in SPH. Beissel and Belytschko (1996) stabilized the nodal integration of Galerkin mesh-free methods by adding the square of the residual of the equilibrium equation to the potential energy. The stabilization term includes second derivatives of shape functions and thus the least squares term serves to stabilize nodal integration. Although, the addition of stabilization term improves the accuracy of solution for the problems with spurious near-singular modes, for problems that do not contain unstable modes in their original solution, this addition actually deteriorate the accuracy. A stabilized conforming nodal integration for Galerkin mesh-free methods was proposed by Chen *et al.* (2001). They identified that for linear exactness in the Galerkin approximation, the shape functions have to be linearly consistent and the nodal integration must satisfy integration constraints. They proposed a strain smoothing stabilization technique to stabilize the nodal integration. The basic idea is to replace the strain at a specific point with the average strain in a Voronoi cell that contains the point. Divergence theorem is then used to replace the area, or volume integration around the point by a contour integration of the Voronoi cell boundary.

In this study, the conventional RBPIM, enriched with polynomial basis functions is implemented for the elastic analysis of discontinues medium. The interface layers between different materials are defined by the concept of linkage element. The stabilized nodal integration technique has been used to integrate the weak form of equations.

RBPIM ENRICHED WITH POLYNOMIAL BASIS FUNCTIONS

A field function $u(x)$ can be approximated using both radial and polynomial basis as:

$$u(x) = \sum_i^n R_i(x)a_i + \sum_j^m P_j(x)b_j = \mathbf{R}^T(x)\mathbf{a} + \mathbf{P}^T(x)\mathbf{b} \quad (1)$$

where, n is the number of field nodes in the local support domain for point \mathbf{x} ; the vector $\mathbf{R}(\mathbf{x})$ is defined as:

$$\mathbf{R}(\mathbf{x}) = [R_1(\mathbf{x}), \dots, R_k(\mathbf{x}), \dots, R_n(\mathbf{x})]^T \quad (2)$$

Where:

$$R_k(\mathbf{x}) = R(r_k) \quad (3)$$

is the radial basis functions and

$$r_k = [(x_k - x)^2 + (y_k - y)^2]^{\frac{1}{2}} \quad (4)$$

is the distance between the point \mathbf{x} and field node X_k ; vector $\mathbf{P}(\mathbf{x})$, where:

$$\mathbf{P}(\mathbf{x}) = [P_1(\mathbf{x}), P_2(\mathbf{x}), \dots, P_m(\mathbf{x})]^T \quad (5)$$

is the vector of polynomial basis functions in 2D space $\mathbf{x}^T = [x, y]$ and m is the number of terms of polynomial basis functions. Vectors \mathbf{a} and \mathbf{b} , where:

$$\mathbf{a} = [a_1, a_2, \dots, a_n]^T \quad (6)$$

$$\mathbf{b} = [b_1, b_2, \dots, b_m]^T \quad (7)$$

are, respectively, coefficients for $\mathbf{R}(\mathbf{x})$ and $\mathbf{P}(\mathbf{x})$. The radial basis functions are used to guarantee the invertability of moment matrix and the polynomial basis functions are used to ensure the linear consistency of generated shape functions. The coefficient vectors \mathbf{a} and \mathbf{b} are determined by enforcing Eq. 1 to be satisfied at all the n nodes within the local support domain. By the lengthy but straightforward procedure given by Liu (2003) we have:

$$u(\mathbf{x}) = \Phi(\mathbf{x})\mathbf{U}_s \quad (8)$$

Where:

$$\mathbf{U}_s = [u_1, u_2, \dots, u_n]^T \quad (9)$$

is a vector of nodal displacements of the nodes in local support domain and

$$\Phi(\mathbf{x}) = [\varphi_1(\mathbf{x}), \varphi_2(\mathbf{x}), \dots, \varphi_n(\mathbf{x})] \quad (10)$$

contains RBPIM shape functions for the n local nodes in which $\varphi_k(\mathbf{x})$ is as follows:

$$\varphi_k(\mathbf{x}) = \sum_i^n R_i(\mathbf{x})S_{aik} + \sum_j^m P_j(\mathbf{x})S_{bjk} \quad (11)$$

where S_{aik} is the (i, k) entry of matrix \mathbf{S}_a where:

$$\mathbf{S}_a = \mathbf{R}_M^{-1} \cdot \mathbf{R}_M^{-1} \mathbf{P}_M \mathbf{S}_b \quad (12)$$

and S_{bjk} is the (j, k) entry of matrix \mathbf{S}_b where:

$$\mathbf{S}_b = (\mathbf{P}_M^T \mathbf{R}_M^{-1} \mathbf{P}_M)^{-1} \mathbf{P}_M^T \mathbf{R}_M^{-1} \quad (13)$$

The moment matrices \mathbf{R}_M and \mathbf{P}_M are consisted of row vectors $\mathbf{R}^T(x_i)$ and $\mathbf{P}^T(x_i)$ ($i = 1, 2, \dots, n$), respectively.

There are many types of radial basis functions. In this study the multi-quadratic form is used as:

$$R(r_i) = (r_i^2 + c^2)^q \tag{14}$$

where, c and q are shape parameters, which are needed to be determined by numerical tests.

VARIATIONAL PRINCIPALS FOR DISCONTINUOUS PROBLEMS

Generally, the total potential energy functional for a discontinuous media is expressed as:

$$\Pi = \Pi_e + \Pi_i + \Pi_f \tag{15}$$

where, Π_e and Π_i are the elastic strain energy of a solid media and interface layer, respectively and Π_f is the potential energy related to external forces. These functionals can be defined as:

$$\Pi_e = \iint_{\Omega} \frac{1}{2} \boldsymbol{\varepsilon}^T \boldsymbol{\sigma} d\Omega \tag{16}$$

$$\Pi_i = \int_{\beta} \frac{1}{2} \boldsymbol{\varepsilon}_i^T \boldsymbol{\sigma}_i d\beta \tag{17}$$

$$\Pi_f = - \int_{\Omega} \mathbf{U}^T \bar{\mathbf{T}} d\Gamma - \iint_{\Omega} \mathbf{U}^T \mathbf{b} d\Omega \tag{18}$$

where, $\boldsymbol{\varepsilon}$ and $\boldsymbol{\sigma}$ are, respectively, the strain and stress tensors of solid domains and $\boldsymbol{\varepsilon}_i$ and $\boldsymbol{\sigma}_i$ are the strain and stress tensors of interface layers between solid domains, respectively. \mathbf{b} is the body force vector, \mathbf{U} is the vector of degrees of freedom, Ω is the problem domain, β is the length parameter along the interface layer, $\bar{\mathbf{T}}$ is the prescribed surface traction and Γ is the boundary along which the surface traction is imposed.

The variational (weak) form of Eq. 15 can be written as:

$$\delta \Pi = \iint_{\Omega} (\delta \boldsymbol{\varepsilon})^T \mathbf{D} \boldsymbol{\varepsilon} d\Omega + \int_{\beta} (\delta \boldsymbol{\varepsilon}_i)^T \mathbf{D}_i \boldsymbol{\varepsilon}_i d\beta - \iint_{\Omega} (\delta \mathbf{U})^T \mathbf{b} d\Omega - \int_{\Gamma} (\delta \mathbf{U})^T \bar{\mathbf{T}} d\Gamma = 0 \tag{19}$$

where, \mathbf{D} and \mathbf{D}_i are the elasticity matrixes of medium and interface layer, respectively.

Using the stress-strain relation, the discrete form of equations can be written as:

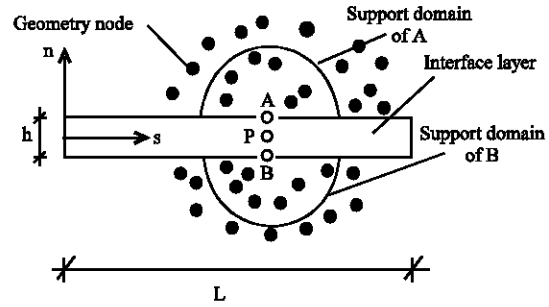


Fig. 1: Interface modeling

$$\mathbf{K}\mathbf{U} = \mathbf{F} \tag{20}$$

Where:

$$\mathbf{K} = \iint_{\Omega} \mathbf{B}^T \mathbf{D} \mathbf{B} d\Omega + \int_{\beta} \mathbf{B}_i^T \mathbf{D}_i \mathbf{B}_i d\beta \tag{21}$$

$$\mathbf{F} = \iint_{\Omega} \Phi^T \mathbf{b} d\Omega + \int_{\Gamma} \Phi^T \bar{\mathbf{T}} d\Gamma \tag{22}$$

where, Φ and \mathbf{B} are, respectively, the shape functions and the gradient of shape functions matrices. Using the generated shape functions, Φ and \mathbf{B} can be constructed as in conventional FEM. Matrices \mathbf{B}_i and \mathbf{D}_i are related to the interface layer. The rest of this section is devoted to the expression of the interface modeling using mesh-free method.

The interface layer is considered as two parallel planes with an insignificant distance from each other. A series of springs are assumed between the planes. The springs are resistant to the relative normal and tangential displacement of planes. The stiffness of springs into the unit area (stiffness coefficient) along normal and tangential directions are k_n and k_s , respectively. As shown in Fig. 1, point P is considered between the planes of the interface layer to determine the strain-displacement relationship. The width of interface (h) is much less than its length (L), hence the strain in the n direction in the interface can be assumed to be constant. The relative displacement of point P can be related to the displacements of point A and B on the top and bottom planes as follows:

$$\boldsymbol{\delta} = [\boldsymbol{\delta}_n \quad \boldsymbol{\delta}_s]^T = \bar{\mathbf{U}}_B - \bar{\mathbf{U}}_A \tag{23}$$

where, $\boldsymbol{\delta}_n$ and $\boldsymbol{\delta}_s$ are the normal and shear relative displacement of point P, respectively and $\bar{\mathbf{U}}_A$ and $\bar{\mathbf{U}}_B$ are displacement vectors of points A and B in local coordinate n - s , respectively. Using the coordinate transform matrix (C) the displacement vectors can be written as:

$$\mathbf{U} = \mathbf{C}\bar{\mathbf{U}} \quad (24)$$

On the other hand, the displacements of points A and B can be related to the displacements of the nodes in the support domain of those points (Fig. 1). So, we have:

$$\begin{aligned} \bar{\mathbf{U}}_A &= \Phi_A \bar{\mathbf{u}}_{gA} \\ \bar{\mathbf{U}}_B &= \Phi_B \bar{\mathbf{u}}_{gB} \end{aligned} \quad (25)$$

where, Φ_A and Φ_B are the shape function matrices of the nodes in the support domains of point A and B respectively and $\bar{\mathbf{u}}_{gA}$ and $\bar{\mathbf{u}}_{gB}$ are the displacement vectors of the nodes in the support domain of A and B, respectively.

Considering Eq. 23-25 we have:

$$\delta = \mathbf{B}_i \mathbf{U}_i \quad (26)$$

Where:

$$\mathbf{B}_i = [-\mathbf{C}\Phi_A \quad \mathbf{C}\Phi_B] \quad (27)$$

$$\mathbf{U}_i^T = [\bar{\mathbf{u}}_{gA}^T \quad \bar{\mathbf{u}}_{gB}^T] \quad (28)$$

Defining the strain tensor in the interface layer as:

$$\varepsilon_i = \{\gamma_{ns} \quad \varepsilon_n\} \quad (29)$$

where, γ_{ns} and ε_n are the shear and normal strain, respectively, we can have:

$$\varepsilon_i = \frac{1}{h} \delta \quad (30)$$

and by combination of Eq. 26 and 30 the strain-displacement relation in the interface layer can be written as follows:

$$\varepsilon_i = \frac{1}{h} \mathbf{B}_i \mathbf{U}_i \quad (31)$$

Considering the strain tensor definition in the interface layer, the stress-strain relation in elastic analysis can be written as:

$$\sigma_i = \mathbf{D}_i (h\varepsilon_i) = \mathbf{D}_i \delta \quad (32)$$

Where:

$$\sigma_i = \{\tau \quad \sigma_n\}^T \quad (33)$$

$$\mathbf{D}_i = \begin{bmatrix} k_s & 0 \\ 0 & k_n \end{bmatrix} \quad (34)$$

where, τ and σ_n are shear and normal stress in the interface layer, respectively.

STABILIZED NODAL INTEGRATION

As noticed before, the source of instability in nodal integration is the vanishing of the first derivatives of the shape functions at the nodes. Therefore attempts have been made either to calculate the derivatives away from the nodes or to derive the formulations in which the derivatives are not manifested. Chen *et al.* (2001) used the latter technique and proposed a strain smoothing as follows:

$$\tilde{\varepsilon}_{ij}^h(\mathbf{x}_L) = \int_{\Omega} \varepsilon_{ij}^h \Psi(\mathbf{x}; \mathbf{x} - \mathbf{x}_L) d\Omega \quad (35)$$

where, ε_{ij}^h is the strain obtained from displacement by compatibility

$$\varepsilon_{ij}^h = \frac{1}{2} \left(\frac{\partial u_i}{\partial x_j} + \frac{\partial u_j}{\partial x_i} \right) \quad (36)$$

and Ψ is a distribution function which is chosen as:

$$\Psi(\mathbf{x}; \mathbf{x} - \mathbf{x}_L) = \begin{cases} \frac{1}{A_L} & \mathbf{x} \in \Omega_L \\ 0 & \mathbf{x} \notin \Omega_L \end{cases} \quad (37)$$

where, A_L is the area of the representative domain of node L obtained from the Voronoi diagram. Combination of Eq. 8 and 35-37 and applying the integration by parts gives:

$$\tilde{\mathbf{\varepsilon}}^h(\mathbf{x}_L) = \sum_{i \in G_L} \tilde{\mathbf{B}}_i(\mathbf{x}_L) \mathbf{U}_i \quad (38)$$

where, G_L is a group of nodes in which their associated shape function supports cover node L. In two dimensional space we have:

$$\tilde{\mathbf{\varepsilon}}^h = \begin{bmatrix} \tilde{\varepsilon}_x^h & \tilde{\varepsilon}_y^h & 2\tilde{\varepsilon}_{xy}^h \end{bmatrix}^T \quad (39)$$

$$\mathbf{U}_i = [\mathbf{U}_{xi}, \mathbf{U}_{yi}]^T \quad (40)$$

$$\tilde{\mathbf{B}}_i(\mathbf{x}_L) = \begin{bmatrix} \tilde{b}_{ix}(\mathbf{x}_L) & 0 \\ 0 & \tilde{b}_{iy}(\mathbf{x}_L) \\ \tilde{b}_{iy}(\mathbf{x}_L) & \tilde{b}_{ix}(\mathbf{x}_L) \end{bmatrix} \quad (41)$$

$$\tilde{b}_{ix}(\mathbf{x}_L) = \frac{1}{A_L} \int_{\Gamma_L} \varphi_i(\mathbf{x}) n_x(\mathbf{x}) d\Gamma \quad (42)$$

$$\tilde{b}_{iy}(x_L) = \frac{1}{A_L} \int_{\Gamma_L} \varphi_i(x) n_y(x) d\Gamma \quad (43)$$

As shown in Fig. 2, Γ_L is the boundary of Voronoi cell which contains node L. n_x and n_y are, respectively, the x and y components of vector \mathbf{n} (outward vector which is normal to boundary of Voronoi cell). Note that in Eq. 41 no derivatives of shape functions are involved in evaluating the smoothed gradient matrix at the nodal points. Considering the Eq. 41 and the nodal integration method, Eq. 21 and 22 can be rewritten as:

$$\mathbf{K}_{ij} = \sum_{L=1}^{NP} \tilde{\mathbf{B}}_i^T(x_L) \mathbf{D} \tilde{\mathbf{B}}_j(x_L) A_L + \mathbf{K}^i \quad (44)$$

$$\mathbf{F}_i = \sum_{L=1}^{NP} \varphi_i(x_L) \mathbf{b} A_L + \sum_{L=1}^{NPb} \varphi_i(x_L) \bar{\mathbf{T}} S_L \quad (45)$$

where, NP is the number points in the local support domain of Node L, NPb is the number of points on the natural boundary, S_L are the weights associated with the boundary points that can also be obtained from the Voronoi diagram and \mathbf{K}^i is the stiffness matrix of the interface layer (second term in Eq. 21).

To calculate Eq. 42 and 43, any numerical integration method can be used, for instance by applying a two-point trapezoidal rule for each segment in Fig. 2, Eq. 42 and 43 can be written as:

$$\tilde{b}_{ix}(x_L) = \frac{1}{A_L} \sum_{M=1}^{N_s} \left[\varphi_i(x_L^M) n_{xL}^M \frac{l_L^M}{2} + \varphi_i(x_L^{M+1}) n_{xL}^M \frac{l_L^M}{2} \right] \quad (46)$$

$$\tilde{b}_{iy}(x_L) = \frac{1}{A_L} \sum_{M=1}^{N_s} \left[\varphi_i(x_L^M) n_{yL}^M \frac{l_L^M}{2} + \varphi_i(x_L^{M+1}) n_{yL}^M \frac{l_L^M}{2} \right] \quad (47)$$

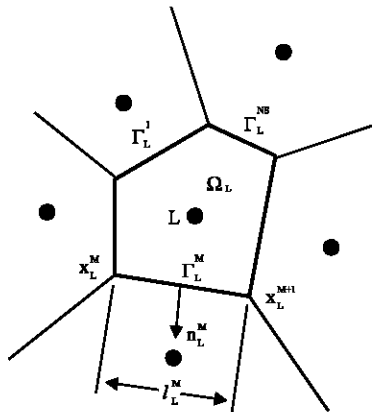


Fig. 2: The Voronoi cell contains node L (Chen *et al.*, 2001)

where, N_s is the total number of segments of Voronoi cell contains node L, x_L^M and x_L^{M+1} are the two end points of boundary segment Γ_L^M and l_L^M is the length of Γ_L^M . n_{xL}^M and n_{yL}^M are, respectively, the x and y components of the outward surface normal of Γ_L^M .

NUMERICAL STUDY

Example 1: Bimaterial bar: Consider a bimaterial bar ($\Omega = \Omega_1 \cup \Omega_2$) as shown in Fig. 3, with length $L = 2$ m, height $h = 8$ m with material moduli E_1 and Poisson ratio ν_1 in Ω_1 and E_2, ν_2 in Ω_2 . The material constants were chosen so that there is no singularity at the edge of the interface; this condition $\frac{E_1}{\nu_1} = \frac{E_2}{\nu_2}$ is for plane stress. Hence, E_1 and ν_1 are, respectively, 20 MPa and 0.2 and E_2 and ν_2 are, respectively, 40 MPa and 0.4. The interface Γ_1 is located in the middle of specimen. For mixed boundary problem with $u_y = 0$ at $y = 0$ and $\sigma_y = \bar{\sigma}$ at $y = h$ and no body force, the exact displacement solution is:

$$u_y(y) = \begin{cases} \frac{\bar{\sigma}}{E_1} y & 0 \leq y \leq \frac{h}{2} \\ \frac{\bar{\sigma}}{E_2} \left(y - \frac{h}{2} \right) + \frac{\bar{\sigma} h}{2E_1} & \frac{h}{2} \leq y \leq h \end{cases} \quad (48)$$

As shown in Fig. 4 three mesh-free models with 30, 90 and 306 nodes in which the distances between nodes are 1, 0.5 and 0.25 meter respectively, are considered. The shear and normal stiffness coefficients of interface are determined by the following equations:

$$k_s = \left(\frac{1}{t} \right) \left(\frac{E_1 + E_2}{2} \right) \left(\frac{1}{2(1 + \frac{\nu_1 + \nu_2}{2})} \right) \quad (49)$$

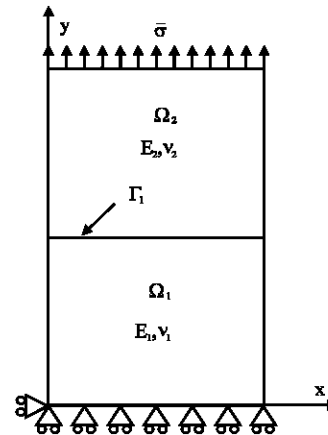


Fig. 3: Bimaterial bar

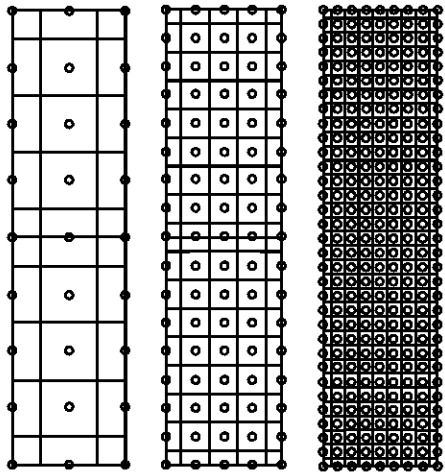


Fig. 4: Mesh-free models for bimaterial bar

$$k_n = \left(\frac{1}{t} \right) \left(\frac{\frac{E_1 + E_2}{2}}{1 - \frac{\nu_1 + \nu_2}{2}} \right) \quad (50)$$

where, k_s and k_n are, respectively, the shear and normal stiffness coefficients and t is the thickness of the interface layer which is chosen 0.005 m. For integration, both, the Gauss and the nodal integration method are used. In Gauss method a 4×16 background mesh with 16 Gauss points in each block and in nodal method the Voronoi diagrams shown in Fig. 4 are employed for integration. Each integration point is employed as the center of circular support domain. To guarantee sufficient and suitable nodes are covered in support domain, the radius of the support domain is specially devised with a slightly adjustable value in the program which is automatically self-tuned such that at least 15 nodes are selected for each local support domain.

In order to compare the results of mesh-free analysis with exact solution, the error indicator in energy is defined as follows:

$$e_n = \frac{\int_{\Omega} (\mathbf{e}^{exact} - \mathbf{e}^{num})^T \mathbf{D} (\mathbf{e}^{exact} - \mathbf{e}^{num}) d\Omega}{\int_{\Omega} (\mathbf{e}^{exact})^T \mathbf{D} \mathbf{e}^{exact} d\Omega} \quad (51)$$

where, \mathbf{D} is the elastic matrix, \mathbf{e}^{exact} and \mathbf{e}^{num} are, respectively, the exact and the mesh-free (numerical) strain tensors. The variation of e_n with nodes distances is shown in Fig. 5 for both methods of integration. As it is obvious, the results of nodal integration are much better than the results of Gauss integration and, they are also in very good agreement with the results of exact solution (i.e., maximum value of e_n for nodal integration is 0.00228).

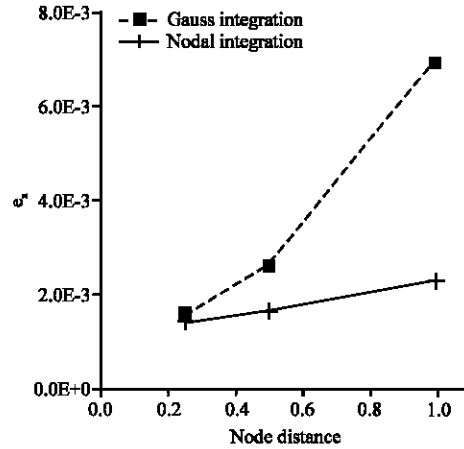


Fig. 5: Variation of e_n with the nodes distances

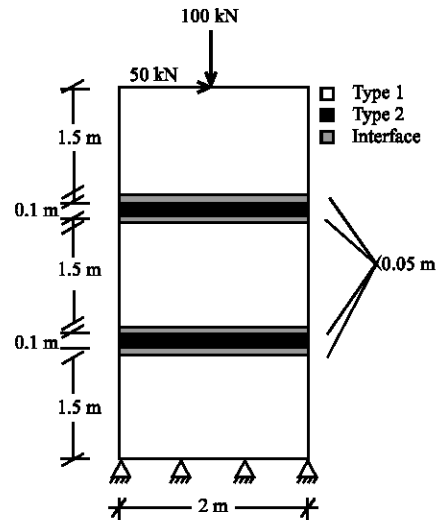


Fig. 6: A column of reinforced elastic material; type 1: material; type 2: two narrow reinforcement strips with the thickness of 0.1 m; Interface: layers with thickness of 0.05 m between materials

The convergence of proposed mesh-free method is also confirmed by decreasing the nodal distance and consequently increasing the accuracy of results.

Example 2: Reinforced column: In this example, an elastic reinforced column is investigated. The dimensions and boundary conditions of the problem are shown in Fig. 6. The elastic modulus of material type1 is 3 GPa and its Poisson's ratio is 0.3. The elastic modulus and Poisson's ratio of material type 2 are 60 and 0.25 GPa, respectively. Interface layers are considered between different materials. The normal and shear stiffness of the interfaces are 10^4 and 10^6 kN m^{-3} , respectively.

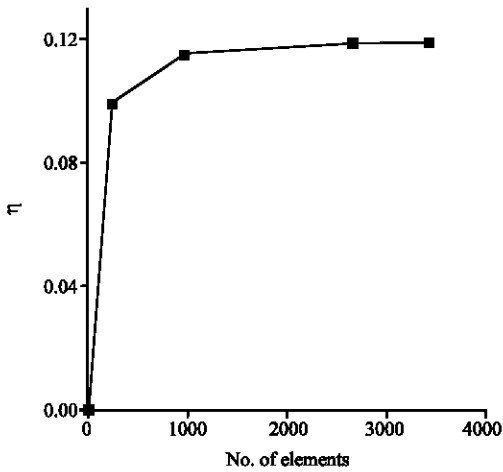


Fig. 7: Variation of η with respect to the number of elements

Since, there is no exact solution for this problem, the FEM is used to compare the results with the mesh-free method. It is assumed that by increasing the number of elements the results of the FEM code gets closer to the exact solution. By increasing the number of elements, a parameter is calculated as:

$$\eta = \frac{\|U_{FEM}^P - U_{FEM}^I\|}{\|U_{FEM}^I\|} \quad (52)$$

where, $\|\cdot\|$ stands for Euclidean norm U_{FEM}^P and U_{FEM}^I are the vectors of displacement for the analysis with P number of elements and the analysis with the initial number of elements, respectively. At any stage of analysis that, by increasing the number of elements the value of η remains constant, the results of the analysis can be assumed to be the best results for the finite element analysis.

In this example, the computer code SIGMAW has been used as the FEM code. The reason for the selection of this software is that it has slip elements and the interface layer can be modeled easily, also the finite element modeling is the most similar to mesh-free simulation. By increasing the number of elements and a comparison of the results with the initial solution, η is calculated at every stage of the analysis. Figure 7 shows the variation of η with respect to the number of elements. According to the Fig. 7, the finite element model with 3420 elements gives the best results.

To investigate the convergence of proposed method, three mesh-free models and their Voronoi diagrams are assumed (Fig. 8). The first model contains 39 nodes which are 1 m apart from each other. In the second and third

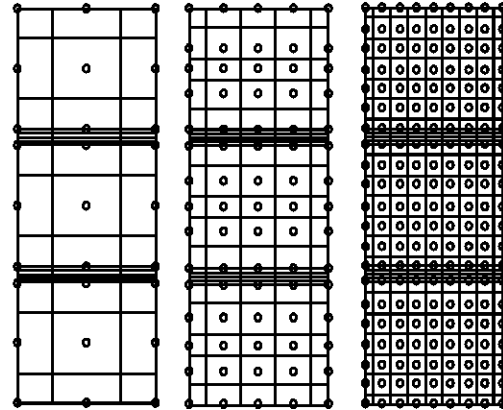


Fig. 8: Mesh-free models for reinforced column

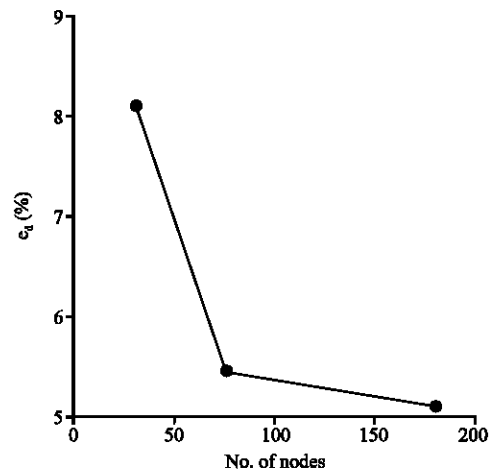


Fig. 9: Variation of e_d with respect to the number of nodes

models the distances between nodes decreased to 0.5 and 0.25 m, respectively and consequently 95 and 225 nodes are generated. The relative error of displacement between the mesh-free and the FEM is determined by:

$$e_d = \sqrt{\frac{\sum (U_{FEM} - U_{MFM})^2}{\sum (U_{FEM})^2}} \quad (53)$$

where, e_d is the relative error of displacement, U_{MFM} is the displacement vector in mesh-free method, U_{FEM} is the displacement vector in FEM. Figure 9 shows the variation of e_d with respect to the distances between nodes. It is obvious that by decreasing the distances between nodes, the relative error is also decreased. This condition confirms the convergence of the method.

To investigate the effect of the size of support domain on the accuracy of results, the values of e_d are plotted against different values of the radiuses of support

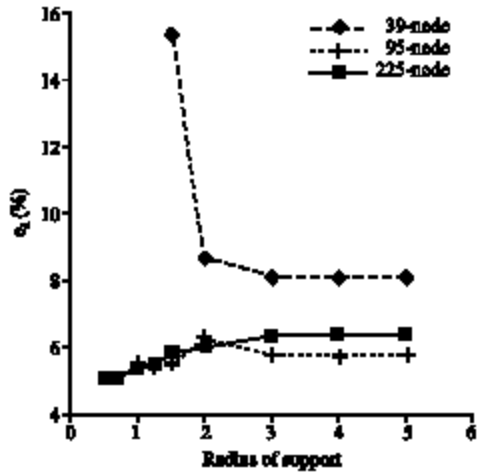


Fig. 10: Variation of e_s with respect to the radiuses of supports

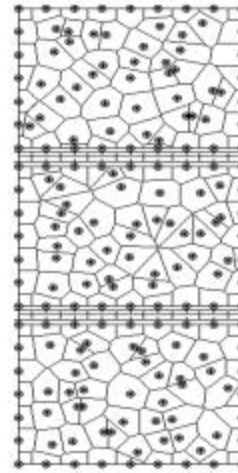


Fig. 12: Irregular nodal arrangement for mesh-free model of reinforced column

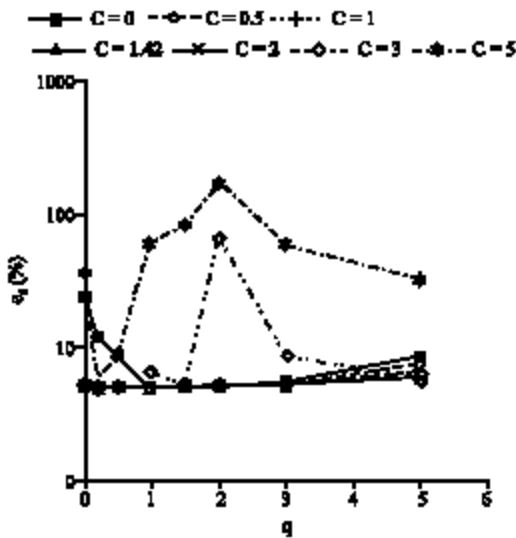


Fig. 11: Effect of shape parameters on the value of e_s

in Fig. 10. Due to the insufficient number of nodes in the support domain, the 39 nodes model has no results for the radiuses value lower than 1.5. On the other hand, as it is obvious from Fig. 10, an increase in the number of nodes in the support domain (i.e., increasing the value of the radius of support) does not necessarily increase the accuracy of results.

The effect of shape parameters on the accuracy of results is investigated by computing e_s for various values of c and q in 225 nodes model at the constant value of radius of support (0.7). The results of analysis are shown in Fig. 11. According to this figure, the analysis is more sensitive to the value of c than to the value of q and for

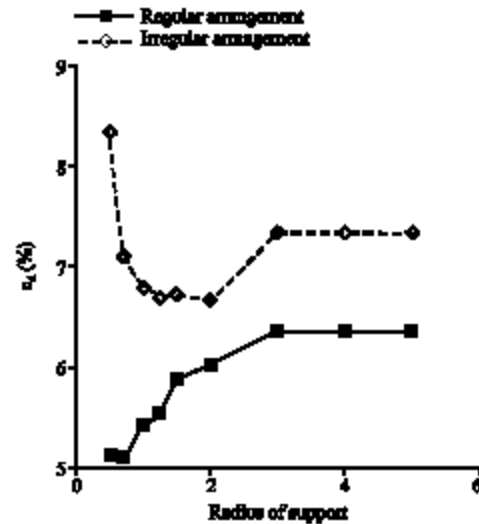


Fig. 13: Effect of nodal arrangement on the value of e_s

the values of c lower than 0.5 or upper than 2, the error increases significantly.

In the last part of this section, the effect of nodal arrangement on the accuracy of results is investigated. Hence an irregular arrangement of nodes is considered for 225 nodes model. This model and the Voronoi cell of each node are shown in Fig. 12. The parameter e_s is calculated for different radiuses of support and the results are shown in Fig. 13 for regular and irregular nodal arrangements. As is obvious from the Fig. 13, the disturbance in nodal arrangement deteriorates the accuracy of results, but the decrease in accuracy is not to the extent to destroy the stability of the proposed method.

CONCLUSION

General conclusions of this study can be expressed as follows:

- A truly mesh-free method is implemented for the elastic analysis of discontinues medium. In this method, the shape functions are constructed by the radial basis point interpolation method which is enriched by polynomial basis terms. The integration is also performed by the nodal method to eliminate the dependency of method to the background mesh.
- The concept of a linkage element is used for interface modeling and the calculations are just based on the displacement of adjacent nodes to the interface layer. So, there is no need of enrichments such as Lagrangian coefficients or penalty method which increase the complexity of solution.
- Comparison of results between two methods of integration showed that the nodal integration impose less errors to the norm of energy (which is an indicator for the numerical error in stress and strain) and hence the accuracy of proposed method is confirmed.
- Suitable choice for the values of shape parameters and the radius of support guarantees the stability of method. This is also true for the irregular arrangement of nodes.

REFERENCES

Atluri, S.N. and T. Zhu, 1998. A new meshless local petrov-Galerkin (MLPG) approach in computational mechanics. *Comput. Mech.*, 22: 117-127.

- Beissel, S. and T. Belytschko, 1996. Nodal integration of the element-free Galerkin method. *Comput. Meth. Applied Mech. Eng.*, 139: 49-71.
- Belytschko, T., Y.Y. Lu and L. Gu, 1994. Element-free Galerkin methods. *Int. J. Numer. Methods Eng.*, 37: 229-256.
- Bonet, J. and S. Kulasegaram, 1999. Correction and stabilization of smooth particle hydrodynamics methods with application in metal forming simulation. *Int. J. Numer. Methods Eng.*, 47: 1189-1214.
- Chen, J.S., C.T. Wu, S. Yoon and Y. You, 2001. A stabilized conforming nodal integration for galerkin mesh-free methods. *Int. J. Numer. Methods Eng.*, 50: 435-466.
- Dolbow, J. and T. Belytschko, 1999. Numerical integration of the galerkin weak form in meshfree methods. *Comput. Mech.*, 23: 219-230.
- Libersky, L.D. and A.G. Petschek, 1991. Smoothed particle hydrodynamics with strength of materials. *Proceeding of the Next Free Lagrange Conference*, June 3-7, Jakson Lake Lodge, Moran, pp: 45-52.
- Liu, G.R. and Y.T. Gu, 2001. A point interpolation method for two-dimensional solid. *Int. J. Numer. Methods Eng.*, 50: 937-951.
- Liu, G.R., 2003. *Meshfree Methods: Moving Beyond the Finite Element Method*. 1st Edn., CRC Press, Boca Raton, ISBN: 0849312388 .
- Liu, W.K., S. Jun and Y.F. Zhang, 1995. Reproducing kernel particle methods. *Int. J. Numer. Methods Eng.*, 20: 1081-1106.
- Randles, P.W., L.D. Libersky and A.G. Petschek, 1999. On neighbors, derivatives and viscosity in particle codes. *Proceedings of ECCM Conference*, 31 August-3 September, Munich, Germany, pp: 1-11.